

A microcomb-empowered Fourier domain mode-locked LiDAR

Zhaoyu Cai,¹ Zihao Wang,¹ Ziqi Wei,¹ Baoqi Shi,^{2,3} Wei Sun,² Changxi Yang,¹ Junqiu Liu,^{2,4} and Chengying Bao^{1,*}

¹State Key Laboratory of Precision Measurement Technology and Instruments,
Department of Precision Instruments, Tsinghua University, Beijing 100084, China.

²International Quantum Academy, Shenzhen 518048, China.

³Department of Optics and Optical Engineering, University of
Science and Technology of China, Hefei, Anhui 230026, China.

⁴Hefei National Laboratory, University of Science and Technology of China, Hefei 230088, China.

Corresponding author: *cbao@tsinghua.edu.cn

Light detection and ranging (LiDAR) has emerged as an indispensable tool in autonomous technology. Among its various techniques, frequency modulated continuous wave (FMCW) LiDAR stands out due to its capability to operate with ultralow return power, immunity to unwanted light, and simultaneous acquisition of distance and velocity. However, achieving a rapid update rate with sub-micron precision remains a challenge for FMCW LiDARs. Here, we present such a LiDAR with a sub-10 nm precision and a 24.6 kHz update rate by combining a broadband Fourier domain mode-locked (FDML) laser with a silicon nitride soliton microcomb. An ultrahigh frequency chirp rate up to 320 PHz/s is linearized by a 50 GHz microcomb to reach this performance. Our theoretical analysis also contributes to resolving the challenge of FMCW velocity measurements with nonlinear frequency sweeps and enables us to realize velocity measurement with an uncertainty below 0.4 mm/s. Our work shows how nanophotonic microcombs can unlock the potential of ultrafast frequency sweeping lasers for applications including LiDAR, optical coherence tomography and sensing.

Photonic integrated circuits (PICs) are playing an increasingly important role in LiDAR technology¹⁻⁴. Besides beam steering, integrated microresonator frequency combs (microcombs)⁵⁻⁷ can be invaluable light sources for LiDARs. Indeed, they have been used for dual-comb ranging^{8,9}, chaotic ranging^{10,11} and parallel frequency-modulated continuous wave (FMCW) ranging¹². In these reports⁸⁻¹², microcombs are usually sent to targets for ranging. Since the power of a microcomb is relatively low, high power amplification is frequently used⁹⁻¹². In this work, we use an integrated silicon nitride (Si_3N_4) microcomb as a frequency ruler at the local site, as opposed to sending to targets, to calibrate a frequency sweep laser for FMCW ranging¹²⁻¹⁹. It not only avoids the power issue, but also leverages the large line spacing of microcombs to calibrate frequency sweeping with ultrahigh chirp rates for ranging. This is because the highest chirp rate that can be calibrated by a comb is limited to $f_r^2/4$ (f_r is the comb repetition rate or line spacing)²⁰.

Calibrating frequency sweeping lasers by optical fre-

quency combs has been widely used for ranging and spectroscopy²⁰⁻²⁷. Compared to interferometer or cavity based frequency calibration methods, combs provide higher accuracy and better immunity to environment fluctuations^{22,23}. Typically, femtosecond laser combs with repetition rates of hundreds of MHz were used for calibration, which limits the chirp rate to a few PHz/s²⁰. Soliton microcombs have been used for laser frequency calibration, but the measured chirp rate was below 12.5 THz/s^{26,27}. Recently, frequency sweep lasers with chirp rates above hundreds of PHz/s have been demonstrated using Fourier domain mode-locked (FDML) lasers²⁸⁻³⁰ and micro-electro-mechanically tuned vertical-cavity surface emitting lasers (MEMS-VCSELs)^{31,32}. These lasers are compelling because their ultrahigh chirp rates and broad bandwidths can boost the FMCW ranging speed, resolution and precision. However, these ultrahigh chirp rate lasers generally sweep in a nonlinear way. Their frequency calibration by microcombs can greatly enhance the functionality in LiDAR, optical coherence tomography (OCT)²⁸, sensing³³ and spectroscopy³⁴.

Here, a Si_3N_4 microcomb³⁵ calibrates the frequency of a broadband FDML laser to reach a normalized ranging precision of $0.27 \text{ nm} \cdot \sqrt{\text{s}}$, an order of magnitude higher than previously reported FMCW LiDARs²³. The highest chirp rate calibrated is 320 PHz/s, which is two orders of magnitude higher than previous reports^{20,23} and highlights the unique advantage of large line spacing microcombs. Additionally, there have been assertions that nonlinear frequency sweeps can obscure velocity measurements, even after calibration³⁶. We show that large chirp rates can mitigate the impact of frequency sweep nonlinearity, and our system achieves velocity measurements with an uncertainty below 0.4 mm/s. Our work also reveals the frequency sweeping dynamics of an FDML laser with an unprecedented bandwidth and resolution.

LiDAR system and 3D imaging. Our LiDAR system is illustrated in Fig. 1a. The FDML laser works by matching the modulation frequency (f_m) of a fibre Fabry-Perot tunable filter (FFP-TF) with the free-spectral-range (FSR) of the cavity²⁸ (see Methods). In such a way, all the lasing frequencies can be stored in the cavity, which avoids the lasing buildup process and enables ultrahigh sweep rates. By carefully managing the dispersion, a lasing bandwidth of 33 nm at a rate of 24.6

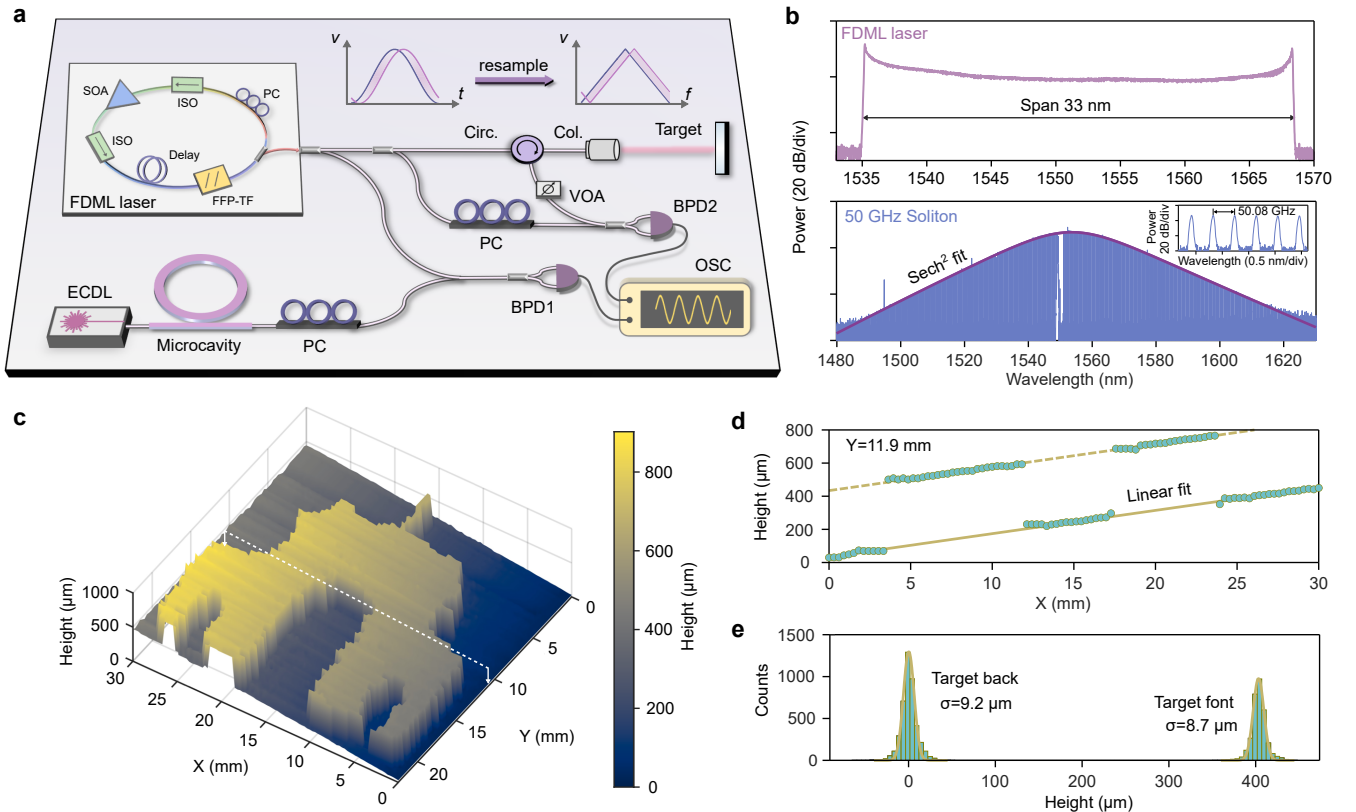


Fig. 1: Architecture of FDML LiDAR and its application in 3D imaging. **a**, Experimental setup of the FDML laser, which is calibrated by an integrated Si_3N_4 soliton microcomb for FMCW ranging. **b**, Optical spectra of the FDML laser and the 50 GHz soliton microcomb. **c**, 3D imaging of a diffusive target representing the Tsinghua Gate, which was slightly tilted in the measurement. **d**, Measured height change of the target and its linear fits along the dashed line in panel **c**. **e**, Distribution of the height after subtracting the solid linear fit.

kHz can be attained (Fig. 1b). Since the tunable filter is driven by a sine-wave, the FDML frequency sweeps in a nonlinear way. To facilitate FMCW ranging, which works by homodyne beat between a frequency sweep laser and its delayed replica with the target (Fig. 1a), we use a Si_3N_4 soliton microcomb with $f_r=50.08$ GHz, whose spectrum is shown in Fig. 1b, to calibrate the FDML frequency in full-time (see Methods).

To showcase the capability of the microcomb-empowered FDML LiDAR, a 3D imaging of the Tsinghua Gate made of diffusive aluminum is presented in Fig. 1c. We scanned the target mechanically for imaging and the received power loss from the target can be as high as 70 dB. The beam steering can be implemented by an optical phase array³ in the future. We deliberately tilted the target to examine the ability of our LiDAR to measure small height changes. Taking the dashed horizontal slice as an example, the measured height along the slice is shown in Fig. 1d, showing a good linearity. By subtracting the solid linear fit in Fig. 1d from the measured height, we have the height distribution shown in Fig. 1e. The standard deviation (σ) is about 9 μm , which mainly results from the surface roughness of the target. An inde-

pendent ranging linearity measurement shows a residual error with $\sigma=0.2$ μm (Extended Data Fig. 1).

Frequency calibration in FMCW ranging. Frequency calibration is essential in the above measurement. We heterodyne beat the FDML laser with the microcomb on a balanced photodetector (BPD) for this calibration. The output was measured by an oscilloscope with a bandwidth of 33 GHz (Tektronix MSO 73304DX). To avoid recording the beat signal with two adjacent lines simultaneously, we set the bandwidth of the oscilloscope to 24 GHz. The beat signal can be frequency-divided to relax the requirement on the digitizer bandwidth. An example of the heterodyne beat signal with over 70 microcomb lines is shown in Fig. 2a, where the shaded region corresponds to the filtered pump and adjacent lines (Methods). Heterodyne beat with a CW laser has been used to study the phase stability of an FDML laser²⁹. Our microcomb enables real-time phase measurements with a much larger bandwidth than the CW laser scheme.

By retrieving the phase of the recorded signal via the Hilbert transform, the instantaneous frequency of the FDML laser can be measured (Methods and Extended Data Fig. 2). We show portions of the instantaneous

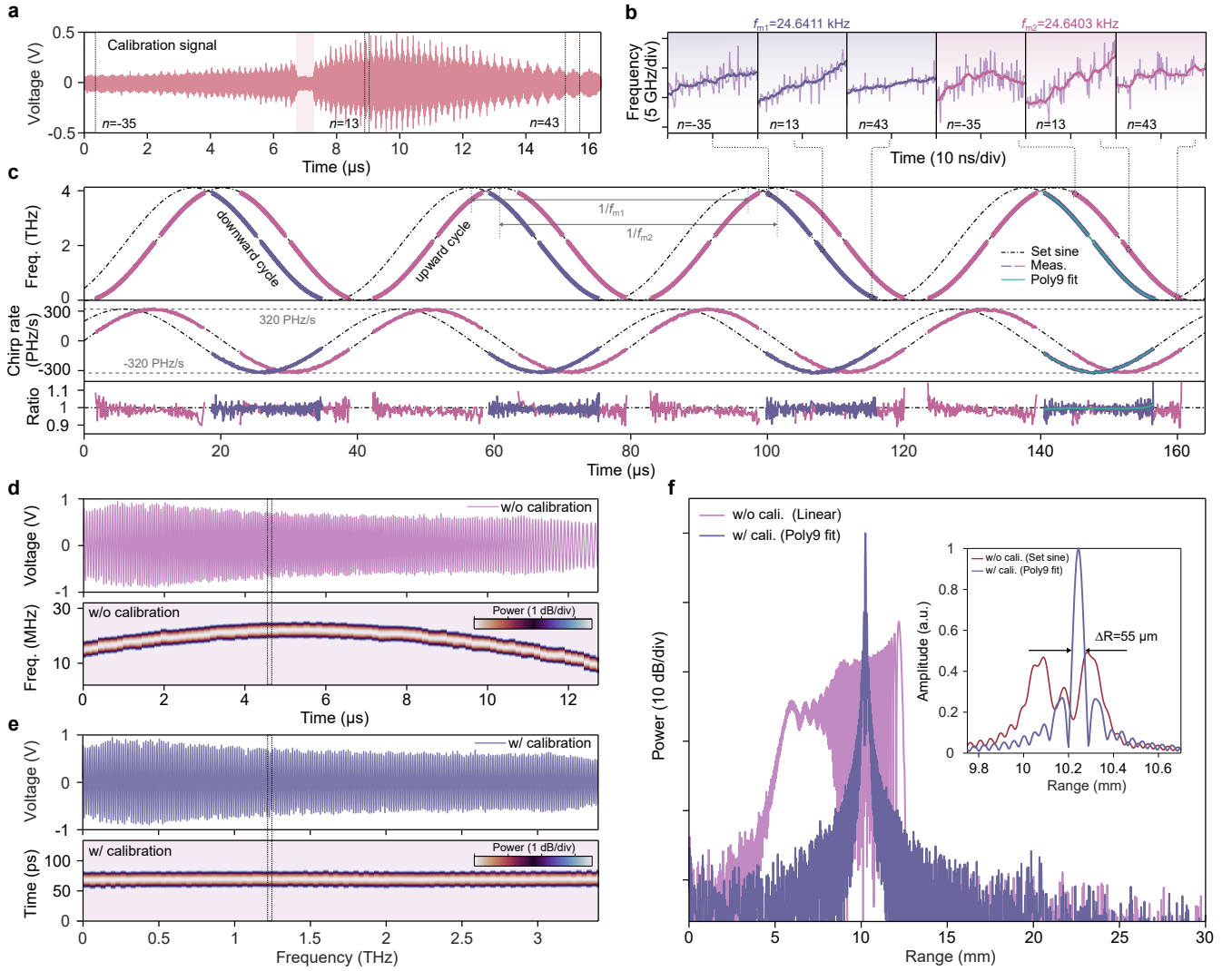


Fig. 2: Microcomb-based frequency calibration for FMCW ranging. **a**, Heterodyne beat signal between the microcomb and the FDML laser. The shaded region corresponds to the filtered pump and adjacent lines. **b**, Portion of the calibrated frequency sweep using three different lines under two drive frequencies f_{m1} and f_{m2} . The light curves are calculated from the direct retrieved phase change, while the dark curves are calculated from phase change smoothed in a 2 ns window. **c**, Top: calibrated frequency change after phase smoothing within the whole frequency sweep span. The green curve is a 9th-order polyfit of the frequency sweep signal. Middle: calibrated chirp rate of the FDML laser. Bottom: ratio between the calibrated chirp rates and chirp rates derived from an assumed sinusoidal frequency sweep. **d**, Measured FMCW ranging signal in the time domain and its instantaneous spectra within a $0.15 \mu\text{s}$ window (dashed lines). **e**, Resampled FMCW signal and the instantaneous spectra. **f**, FMCW ranging output when using the direct measured signal and the resampled data. The inset shows the linear ranging outputs using the microcomb frequency calibration and an assumed sine-wave for resampling.

frequency change measured by 3 different comb lines in Fig. 2b (n is the comb line number with respect to the pump). For two modulation frequencies $f_{m1}=24.6411$ kHz and $f_{m2}=24.6403$ kHz, the instantaneous frequencies change distinctively. For f_{m1} , there are abrupt frequency jumps at a frequency of about 0.8 GHz, while the frequency spurs occur almost irregularly for f_{m2} (Extended Data Fig. 3). By smoothing the measured phase in a 2 ns time window, the spurs can be averaged and the smoothed frequency sweeps are plotted as the dark blue

and pink curves in Fig. 2b. The smoothed frequency sweeps over the full FDML lasing span are plotted in Fig. 2c. Note that FDML lasing exists in both the upward and the downward sweep cycles for f_{m2} , while it only exists in the downward cycle for f_{m1} . Similar lasing asymmetry was reported in ref.³⁷. The chirp rates were also calculated and plotted in Fig. 2c. In general, both the laser frequency and the chirp rate track sine-waves set at $f_{m1,2}$. When normalizing the calibrated chirp rates by the assumed sine-waves, we can observe the chirp rate ac-

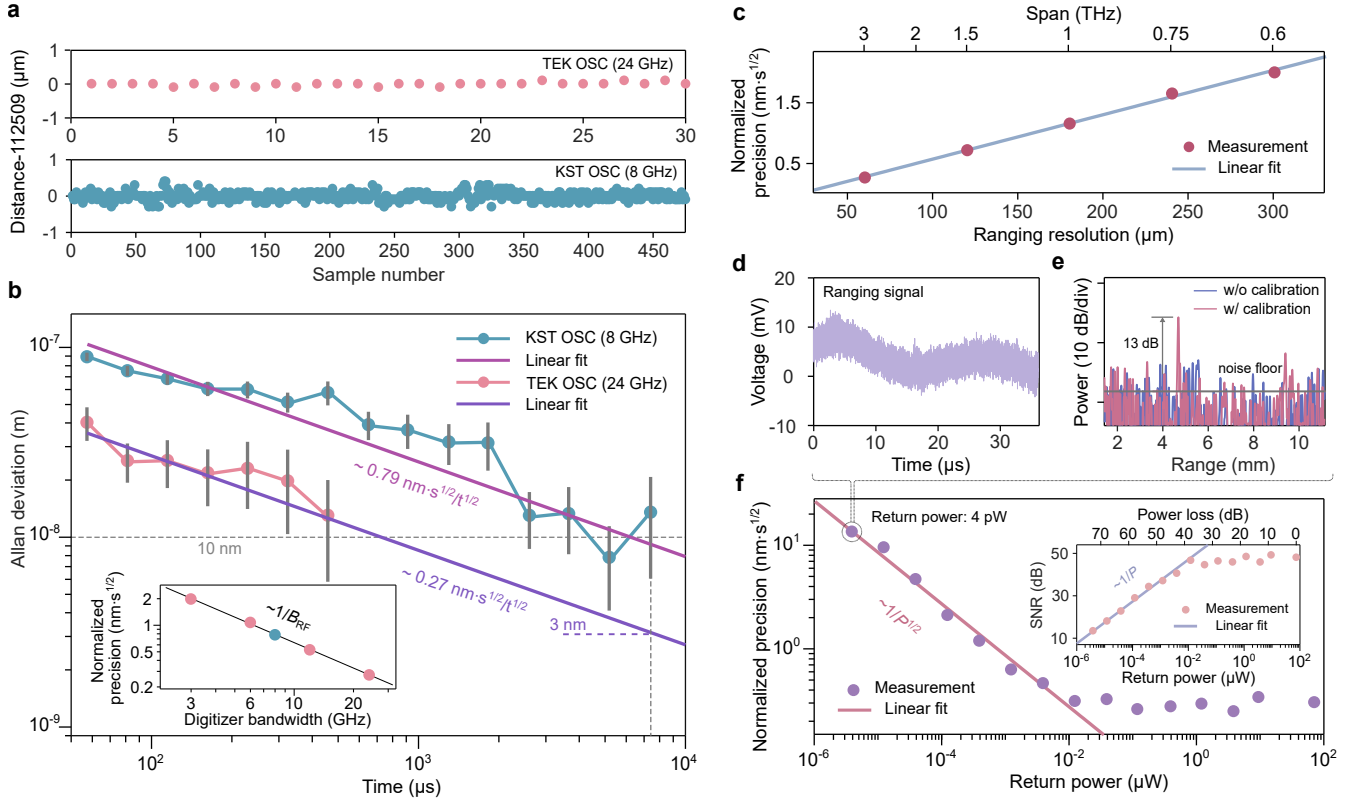


Fig. 3: Precision of the FDML LiDAR. **a**, Distance in multiple measurements when the calibration signal was recorded by a 33 GHz oscilloscope and a 8 GHz oscilloscope. The 8 GHz oscilloscope has a larger memory depth and recorded data for a longer time. **b**, Allan deviation of the measured distance, which scale as $t^{-1/2}$ with the averaging time t . Sub-10 nm precision is achieved in less than 10 ms. The inset shows normalized precision scales as $1/B_{RF}$ with B_{RF} being the digitizer bandwidth. **c**, Normalized precision scales linearly with the ranging resolution. **d**, Time domain FMCW ranging signal with a return power of 4 pW. **e**, FMCW ranging output using the direct time domain signal and the microcomb-calibrated signal with a 4 pW return power. **f**, Measured normalized ranging precision with different return powers (local oscillator power was 75 μ W). The normalized precision scales as $P^{-1/2}$ for return powers $P < 10$ nW. The inset shows SNR under different return powers.

tually deviates from the set sweep, and the deviation is stronger at the edges of the frequency sweep span. Frequency sweep manner is also observed to be different in different modulation cycles. Microcombs can be used as a tool to better understand the ultrafast sweeping FDML or MEMS-VCSEL lasing dynamics in future work.

Since the instantaneous frequency change is steadier for f_{m1} , we used this frequency for the ranging experiments. The temporal ranging signal recorded by BPD2 (see Fig. 1a) is shown in Fig. 2d. As the output of BPD2 was low-pass filtered by a 100 MHz filter, the frequency spurs in Fig. 2b do not impact this signal. When gating the signal by a 0.15 μ s window (dashed lines in Fig. 2d) to look into the instantaneous spectra, time-varying frequency is observed. Since the smoothed frequency sweep in Fig. 2b is still influenced by the frequency spurs, we further used the 9th-order polyfit to fit the frequency sweep (green curves in Fig. 2c). Then, the fitted frequencies were used to resample the FMCW ranging signal in the frequency domain (Methods)²³. The resam-

pled instantaneous oscillation ‘frequency’ becomes uniform (Fig. 2e). By Fourier transforming the resampled signal, we obtained the ranging signal in Fig. 2f. A sharp peak centered at 10.2 mm with a resolution of 55 μ m can be observed. When zooming in the peak in a linear scale, a transform-limited signal can be observed. In contrast, if we Fourier transform the time-domain signal directly, the ranging spectrum is broad and meaningless. As the FDML laser was driven by a sine-wave, we also assumed the FDML lasing frequency changes in a sinusoidal way with the frequency set at f_{m1} and the starting/ending frequency read from the optical spectrum. When resampling the time-domain signal by this assumed sine-wave, the Fourier transformed signal is still broad (inset of Fig. 2f). Therefore, it is critical to have the FDML laser precisely calibrated for ranging, and we have an ultrahigh chirp rate of 320 PHz/s calibrated for FMCW ranging.

High precision FMCW ranging. Precise frequency calibration and broad bandwidth of the FDML laser enable sub-10 nm precision. We show the continuously mea-

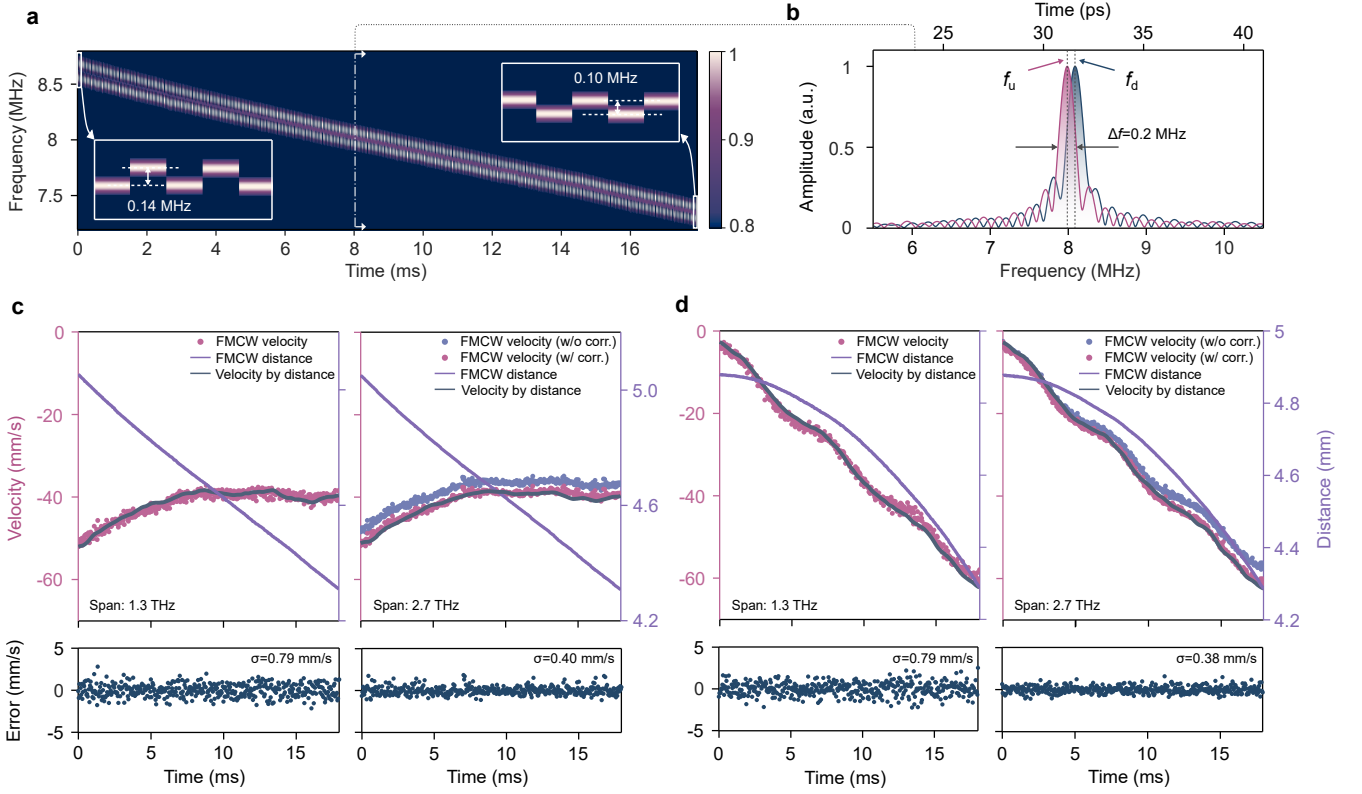


Fig. 4: Velocity measurements using the FDML LiDAR. **a**, Continuous ranging spectra featuring a decrease in mean frequency and frequency difference, indicating a deceleration motion of the target. **b**, Ranging spectra at 8 ms of panel **a** in a linear scale (using a 1.3 THz lasing bandwidth). **c**, **d** FMCW measured velocity and velocity calculated from the measured distance. The bottom panels are residual error between the FMCW velocity and its polyfit. When using 2.7 THz lasing bandwidth for measurement, a correction factor should be included, due to the strong frequency sweep nonlinearity. Data were measured by the 8 GHz Keysight oscilloscope.

sured distance in Fig. 3a. Since the 33 GHz oscilloscope has a limited memory depth, we also used a 8 GHz oscilloscope (Keysight DSOS804A) to record the FMCW ranging signal in a longer time. The corresponding Allan deviation is plotted in Fig. 3b. The precision scales as $0.27 \text{ nm} \cdot \sqrt{s}/t^{1/2}$ and $0.79 \text{ nm} \cdot \sqrt{s}/t^{1/2}$ (t is the measurement time), respectively. Since the 8 GHz oscilloscope only calibrate the FDML laser in about a third of the frequency span, the precision is worse than the 33 GHz oscilloscope data. Despite the limited bandwidth, the results obtained by the 8 GHz oscilloscope still reaches sub-10 nm precision in 5 ms. Furthermore, it shows the Allan deviation keeps converging in at least 8 ms. Hence, we believe that our FMCW LiDAR can reach a precision of 3.0 nm at 8 ms, once sufficiently long data are recorded.

We further low-pass filtered the 33 GHz oscilloscope recorded data by different bandwidth B_{RF} to analyze the ranging precision. The normalized precision scales as $1/B_{RF}$ and the 8 GHz oscilloscope data also aligns with the scaling (inset of Fig. 3b). Therefore, only the calibrated frequencies contribute to the improvement of the ranging precision. This means full-time frequency calibration is more advantageous than only using combs for tick-like calibration^{21,27}.

As noted in ref.³⁸, ranging precision is proportional to $\Delta R/\sqrt{\text{SNR}}$, where ΔR is the resolution and SNR is the signal-to-noise ratio in the power spectrum of the ranging signal. By selecting different frequency spans of the calibrated signal in Fig. 2e, we derive the normalized precision under different resolutions (Fig. 3c). As expected, a linear relationship with ranging resolution ΔR is observed. To further examine the dependence on SNR, we attenuated the received power to measure the ranging precision (see Fig. 1a). When reducing the power to 4 pW (that is about 600 photons in the used downward sweep cycle and 72 dB loss in the signal arm), the recorded signal in the time domain almost shows no interferometric features. In the ‘ranging’ domain, a peak with SNR of 13 dB can still be observed. No such peak can be observed when the frequency sweep is not calibrated. The normalized precision in this case is $13 \text{ nm} \cdot \sqrt{s}$. When increasing the received power, the normalized Allan deviation decreases in an inverse square-root way, as the SNR is determined by the product of the local and received powers (Fig. 3f and its inset). Ranging precision and SNR saturate for received power above 10 nW, which may be attributed to the spurious reflections in the fibres²³. Once the parasitic reflections dominate the

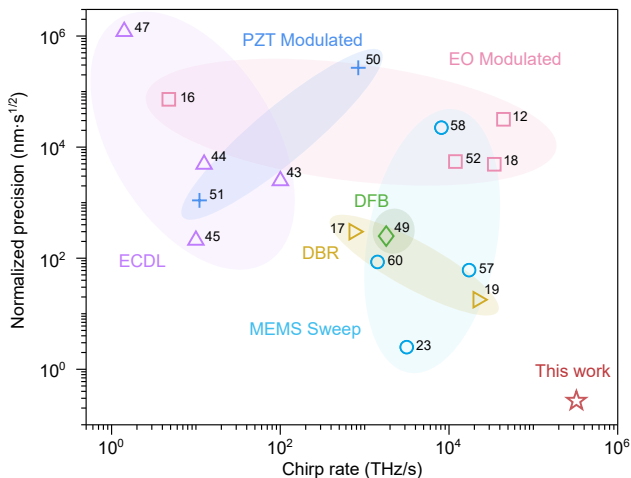


Fig. 5: FDML LiDAR performance in comparison with other reports. Our system has an excellent combination of normalized precision and chirp rate.

noise floor, increasing received power no longer improves the SNR and the precision is clamped.

Velocity measurements. Doppler frequency shift from a moving target causes frequency split in the FMCW ranging spectra for the upward and downward sweep cycles. With frequency calibration and data resampling, the ranging spectrum has a time-axis (Figs. 2e, f) rather than a frequency-axis. The time-axis should be converted back to a frequency-axis to locate the two split frequency peaks f_u and f_d for velocity measurements. Artifacts can arise in the conversion with nonlinear frequency sweeps. Large chirp rates help mitigate the artifacts (Methods).

In this experiment, we set the drive frequency at f_{m2} to have FDML lasing in both sweep cycles. The continuous ranging spectra measured from a moving target is shown in Fig. 4a (recorded by the 8 GHz oscilloscope). The inset clearly shows the frequency split and the deceleration of the target. The ranging spectra at 8 ms are plotted in Fig. 4b, indicating that both the upward and the downward cycles are calibrated to have transform-limited ranging signals. We use a relatively sweep bandwidth of 1.3 THz for this measurement so as to lower the frequency sweep nonlinearity, and the time-axis is transferred to the frequency-axis by simply multiplying the overall chirp rate (Methods).

We show the distance and velocity measured in real-time in Figs. 4c, d, corresponding to a deceleration and an acceleration scenario, respectively. The FMCW measured velocity agrees well with the velocity calculated from the measured distance. The residual error between the FMCW measured velocities and their polyfit has a standard deviation as small as 0.79 mm/s. This velocity uncertainty can be further reduced to 0.40 mm/s by using a 2.7 THz bandwidth for measurement. With this broader bandwidth, the frequency sweep nonlinearity becomes larger and a correction factor should be included (Figs. 4c, d), see Methods and Extended Data Fig. 4 for

details. The velocity uncertainty is fairly low considering the ultrahigh chirp rate, which extends the range of measurable velocity but adds difficulty in measuring velocity precisely (Methods and Extended Data Table 1).

Discussions. Our work establishes a technique to tame ultrafast frequency sweep lasers (theoretically up to chirp rates of hundreds of EHz/s) for FMCW LiDAR with low return power. A PIC-based microcomb calibrates a broadband FDML laser with ultrahigh chirp rates to reach the best normalized precision for FMCW LiDARs at an update rate of 24.6 kHz (Fig. 5 and Extended Data Table 1). FDML lasers with lasing bandwidth exceeding 20 THz and MHz update rates have been demonstrated³⁹. Together with a dispersion-engineered, broadband microcomb, it may further improve the ranging precision and measurement speed. Although the absolute distance in FMCW LiDARs can be adjusted by tuning the length of the reference arm, the measurement range is limited by the linewidth of the frequency sweeping laser. Our FFP-TF has a relatively broad bandwidth, which limits this range to about ten centimetre. Hence, the current system may be more suitable for fast 4D imaging (including velocity) applications. By optimizing the dispersion management and controlling f_m precisely, the coherence length of an FDML laser can reach metre-scale⁴⁰. This requires meticulous control of the laser configuration. Frequency sweep dynamics revealed by the microcomb can be used in turn to optimize the laser condition. MEMS-VCSEL lasers with ultrahigh chirp rates and narrow linewidths can pair with microcombs similarly to extend the measurement range to hundreds of metres³¹. Finally, our work can guide precise FMCW velocity measurement with frequency sweep nonlinearity.

Methods

Fourier domain mode-locked laser. The FDML laser consists of a FFP-TF (MOI-FFP-TF2-1520-1570-7.5G2000) with a finesse of 2000 and an FSR of 135 nm, a semiconductor optical amplifier (Thorlabs SOA117S), a fibre delay of 8.1 km consisting of a 0.9 km dispersion compensation fibre (DCF) and a 7.2 km single mode fibre (SMF). Two optical isolators were used to ensure unidirectional operation and a polarization controller (PC) was used to optimize the lasing polarization. A pulse shaper (Finisar WS 1000B) was inserted for finer dispersion compensation. The filter was driven by a sinusoidal signal around 24.6 kHz, and the output was derived from the 30%-port of a 70/30 coupler. The output power of the laser was about 1.3 mW, which is mainly limited by the damage power of the filter.

Silicon nitride soliton microcomb. The foundry manufactured Si_3N_4 microresonator has a dimension of $0.81 \times 2.2 \mu\text{m}^2$ ³⁵. The intrinsic and loaded Q-factors of the sample are 9.8 million and 6.4 million, respectively. An external cavity diode laser (ECDL, Toptica CTL1550) was amplified to pump the microresonator with an on-chip power of 200 mW. To mitigate the thermal instability, we used a single-sideband modulator (SSBM) based fast laser sweep technique to initiate the soliton generation^{41,42}. To avoid the influence of the residual sidebands from the SSBM, we suppressed the frequencies near the pump by a notch filter with a bandwidth

of 200 GHz (4 lines). The heterodyne beat between the soliton microcomb and the FDML laser was registered by a BPD (Finisar BPDV2150R) with a bandwidth of 43 GHz, whose output was amplified by a low noise amplifier.

Phase retrieval and frequency calibration. The phase retrieval process is also described in Extended Data Fig. 2. We first separated the measured heterodyne beat signal into different segments (each lasting 4.6 ns). Then, we Fourier transformed the segmented data and filtered out the strong peaks by a bandwidth of 3.5 GHz (Extended Data Fig. 2b). The filtered spectrum was inverse Fourier transform back to the time domain. Phase of the filtered signal was retrieved by Hilbert transform (Extended Data Fig. 2c). The phase was further smoothed in a 2 ns window to yield the instantaneous frequency (Extended Data Figs. 2d, e). Then the heterodyne frequency results is unwrapped by the comb spacing $f_r=50.08$ GHz to yield FDML laser instantaneous frequency in the full sweep span (Extended Data Fig. 2f).

Resampling of the ranging signal. For a distance R , the round trip time delay is $\Delta t = 2R/c$, where c is the light velocity in the air. We can write the local and signal frequency sweep field as $E_{LO}(t) = E_1(t)\exp[i\varphi(t)]$ and $E_{sig} = E_2(t + \Delta t)\exp[i\varphi(t + \Delta t)]$, where $E_{1(2)}$ is the laser amplitude, and $\varphi(t)$ include the phase change due to the sweeping frequency. Since resampling mainly deals with the phase of the measured time domain signal, we first omitted the possible amplitude variation in the laser field. Then, the normalized output of BPD2 in Fig. 1a can be written as,

$$V_r(t) = \cos[\varphi(t + \Delta t) - \varphi(t)]. \quad (1)$$

Since the FDML laser sweeps in a nonlinear way, the instantaneous frequency of $V_r(t)$ (from a static target) is time varying and can be written as,

$$f_b(t) = \frac{1}{2\pi} \frac{d[\varphi(t + \Delta t) - \varphi(t)]}{dt} = \nu(t + \Delta t) - \nu(t) \approx \Delta t \cdot d\nu(t)/dt, \quad (2)$$

where $\nu(t)$ is the instantaneous frequency of the FDML laser. Eq. 2 holds when Δt is relatively small.

Thus, $\varphi(t + \Delta t) - \varphi(t)$ can be calculated as,

$$\varphi(t + \Delta t) - \varphi(t) = 2\pi \int_0^t f_b(\tau) d\tau \approx 2\pi \Delta t [\nu(t) - \nu(0)]. \quad (3)$$

The ranging signal can be written as,

$$V_r(t) = \cos(2\pi \Delta t [\nu(t) - \nu(0)]) = \cos(2\pi \Delta t \nu_s(t)), \quad (4)$$

where we define $\nu_s(t) \equiv \nu(t) - \nu(0)$. By replacing the time-axis with the frequency-axis, the signal $V_r(t)$ is resampled as $V_r(\nu_s)$. Then, Δt can be derived via Fourier transform versus ν_s . In the Fourier transform, we added zeros, whose length is nine times of the recorded data length, to the resampled data so as to locate the peak and Δt more accurately.

Velocity measurement. When the target is moving, the beating frequency $f_b(t)$ becomes,

$$f_b(t) \approx \Delta t \cdot d\nu(t)/dt + f_D, \quad (5)$$

where $f_D = v/\lambda_c$ and v is the velocity being measured. Thus, the phase difference $\varphi(t + \Delta t) - \varphi(t)$ becomes,

$$\varphi(t + \Delta t) - \varphi(t) \approx 2\pi \Delta t \nu_s(t) + 2\pi f_D t. \quad (6)$$

$\nu_s(t)$ is positive (negative) in the upward (downward) cycle. We focus on the positive frequencies in the following analysis and write the complex form of $V_r(t)$ as,

$$V_r(t) = \underbrace{\exp(i2\pi \Delta t |\nu_s(t)|)}_{V_{r1}} \underbrace{\exp(\pm i2\pi f_D t)}_{V_{r2}}. \quad (7)$$

The ranging spectrum is $\tilde{V}_{r1} \otimes \tilde{V}_{r2}$, where $\tilde{V}_{r1(r2)}$ is the spectrum for $V_{r1(r2)}$ and \otimes is the symbol for convolution. In a linear sweep case, $\nu(t) = \nu(0) + \nu_1 t$, where ν_1 is the chirp rate. Resampling is not needed, and the ranging spectrum is,

$$\tilde{V}_r(f) = \delta(|\nu_1| \Delta t) \otimes \delta(\pm f_D) = \delta(|\nu_1| \Delta t \pm f_D). \quad (8)$$

Therefore, the ranging peaks are shifted by $\pm f_D$ (i.e., spaced by $2f_D$).

In a nonlinear sweep case, we define the relationship that $\nu_s(t) \equiv \nu_1 t + \nu_e(t)$, where $\nu_1 = (\nu(T) - \nu(0))/T$ (T is the ending time of frequency sweep) is the overall chirp rate and ν_e is an error frequency. Then, $V_r(t)$ is resampled as,

$$V_r(\nu_s) = \underbrace{\exp(i2\pi \Delta t |\nu_s|)}_{V_{r1}} \underbrace{\exp(\pm i2\pi f_D \nu_s / \nu_1)}_{V_{r2}} \underbrace{\exp(\pm i2\pi f_D \nu_e / \nu_1)}_{V_{r3}}. \quad (9)$$

Fourier transform versus ν_s yields the ranging spectrum as,

$$\tilde{V}_r(t) = \delta(\Delta t) \otimes \delta(\pm f_D / \nu_1) \otimes \tilde{V}_{r3}(t) = \delta(\Delta t \pm f_D / \nu_1) \otimes \tilde{V}_{r3}(t). \quad (10)$$

When $f_D \nu_e / \nu_1$ is small, $V_{r3}(\nu_s)$ can be approximated as a constant ($\tilde{V}_{r3}(t) = \delta(0)$). Then, $\tilde{V}_r(t)$ still recovers f_D and velocity (1.3 THz case in Fig. 4). Therefore, velocity measurement works better, when the velocity is low (small f_D) and selecting a relatively small optical bandwidth (small ν_e). Moreover, the ultrahigh chirp rate of FDML lasers (large ν_1) is beneficial for velocity measurement with frequency sweep nonlinearity and data resampling.

When $f_D \nu_e / \nu_1$ is large, $\tilde{V}_{r3}(t)$ may distort the velocity measurement. Since $\nu_s(t)$ has been measured accurately by the microcomb, $\tilde{V}_{r3}(t)$ can be calculated numerically with some prior knowledge of f_D , which can be attained by using a small frequency sweep bandwidth first. Then its influence can be corrected (Extended Data Fig. 4).

Eq. 10 shows uncertainty in Δt is multiplied by ν_1 when determining f_D , which means measuring velocity precisely is challenging for large chirp rates. The largest f_D that can be measured is $\nu_1 \Delta t$; and the measurable velocity is limited to $v_{\max} = \lambda_c \nu_1 \Delta t$.

Data Availability The data that support the plots within this paper and other findings are available.

Code Availability The code that supports findings of this study are available from the corresponding author upon request.

Acknowledgements We thank Prof. Qiang Liu and Prof. Yidong Tan at Tsinghua University for discussions and equipment loan. The silicon nitride chip used in this work was fabricated by Qaleido Photonics. This work is supported by the National Key R&D Program of China (2021YFB2801200), by the National Natural Science Foundation of China (62250071, 62175127), by the Tsinghua-Toyota Joint Research Fund, and by the Tsinghua University Initiative Scientific Research Program (20221080069).

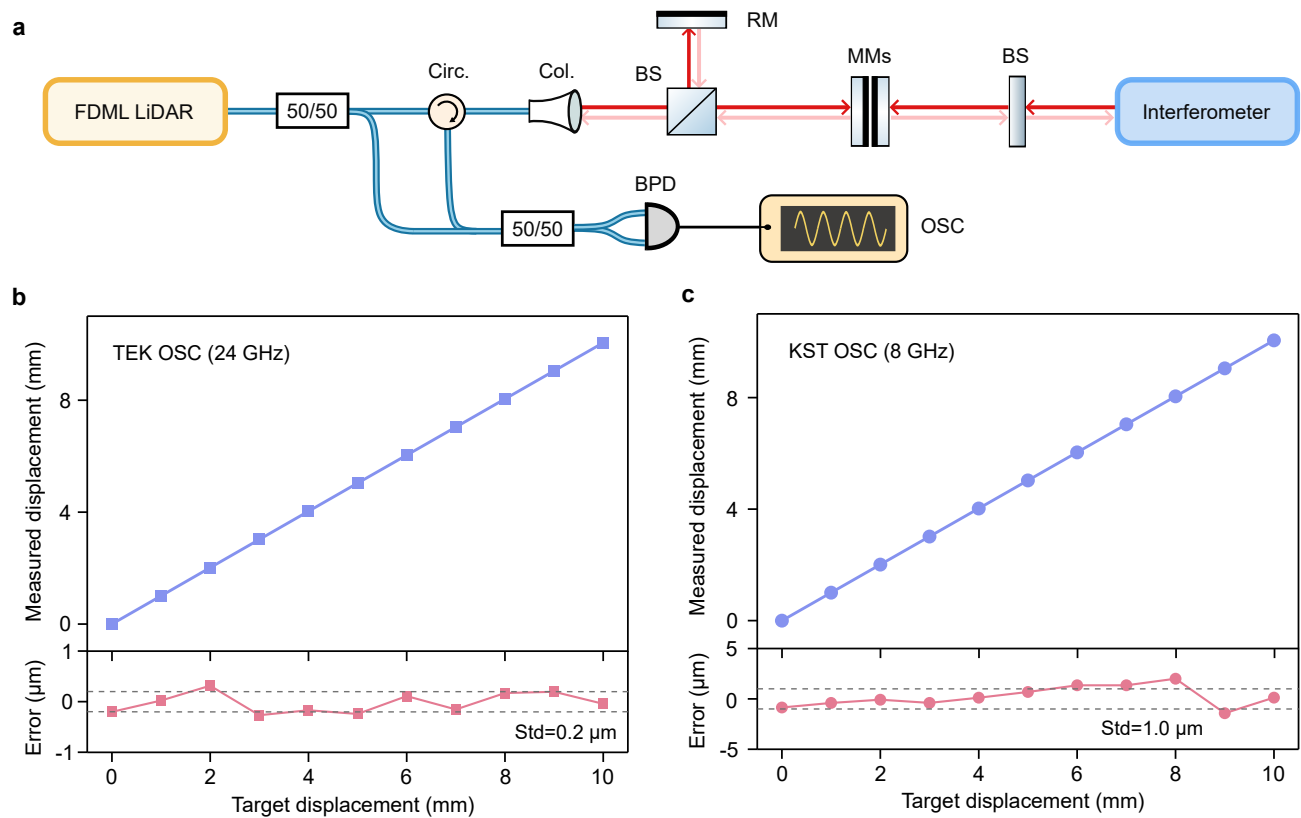
J.L. acknowledges support from the National Natural Science Foundation of China (12261131503), Innovation Program for Quantum Science and Technology (2023ZD0301500), Shenzhen-Hong Kong Cooperation Zone for Technology and Innovation (HZQB-KCZYB2020050), and Shenzhen Science and Technology Program (RCJC20231211090042078).

Author Contributions Z.C. led the experiments with assistance from Z. Wang., Z. Wei, and C.Y.; B.S., W.S. and J.L. prepared and characterized the Si₃N₄ chip. The project was supervised by C.B.

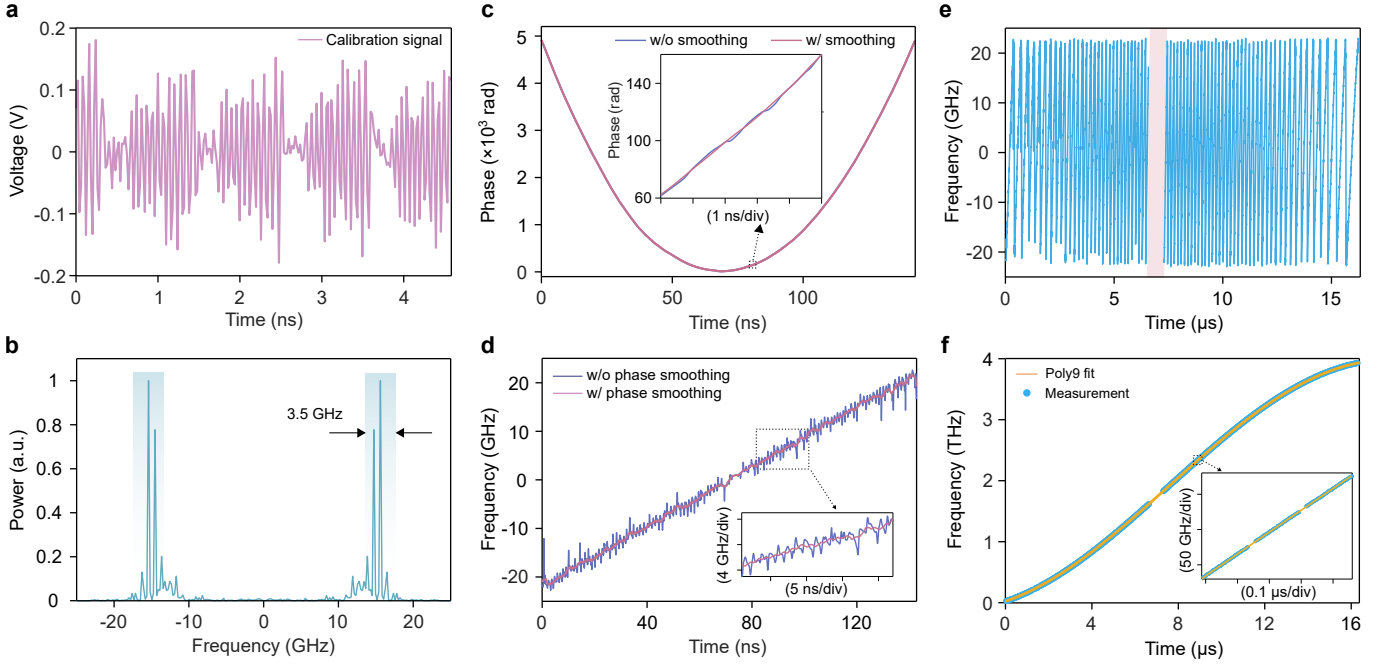
Competing Interests The authors declare no competing interests.

- ¹ Kim, I. *et al.* Nanophotonics for light detection and ranging technology. *Nature Nanotechnology* **16**, 508–524 (2021).
- ² Sun, J., Timurdogan, E., Yaacobi, A., Hosseini, E. S. & Watts, M. R. Large-scale nanophotonic phased array. *Nature* **493**, 195–199 (2013).
- ³ Poulton, C. V. *et al.* Coherent solid-state LIDAR with silicon photonic optical phased arrays. *Opt. Lett.* **42**, 4091–4094 (2017).
- ⁴ Zhang, X., Kwon, K., Henriksson, J., Luo, J. & Wu, M. C. A large-scale microelectromechanical-systems-based silicon photonics LiDAR. *Nature* **603**, 253–258 (2022).
- ⁵ Herr, T. *et al.* Temporal solitons in optical microresonators. *Nature Photonics* **8**, 145 (2014).
- ⁶ Kippenberg, T. J., Gaeta, A. L., Lipson, M. & Gorodetsky, M. L. Dissipative Kerr solitons in optical microresonators. *Science* **361**, eaan8083 (2018).
- ⁷ Chang, L., Liu, S. & Bowers, J. E. Integrated optical frequency comb technologies. *Nature Photonics* **16**, 95–108 (2022).
- ⁸ Suh, M.-G. & Vahala, K. J. Soliton microcomb range measurement. *Science* **359**, 884–887 (2018).
- ⁹ Trocha, P. *et al.* Ultrafast optical ranging using microresonator soliton frequency combs. *Science* **359**, 887–891 (2018).
- ¹⁰ Chen, R. *et al.* Breaking the temporal and frequency congestion of LiDAR by parallel chaos. *Nature Photonics* **17**, 306–314 (2023).
- ¹¹ Lukashchuk, A., Riemensberger, J., Tusnín, A., Liu, J. & Kippenberg, T. J. Chaotic microcomb-based parallel ranging. *Nature Photonics* **17**, 814–821 (2023).
- ¹² Riemensberger, J. *et al.* Massively parallel coherent laser ranging using a soliton microcomb. *Nature* **581**, 164–170 (2020).
- ¹³ Behroozpour, B., Sandborn, P. A., Wu, M. C. & Boser, B. E. Lidar system architectures and circuits. *IEEE Communications Magazine* **55**, 135–142 (2017).
- ¹⁴ Lihachev, G. *et al.* Low-noise frequency-agile photonic integrated lasers for coherent ranging. *Nature Communications* **13**, 3522 (2022).
- ¹⁵ Snigirev, V. *et al.* Ultrafast tunable lasers using lithium niobate integrated photonics. *Nature* **615**, 411–417 (2023).
- ¹⁶ Rogers, C. *et al.* A universal 3D imaging sensor on a silicon photonics platform. *Nature* **590**, 256–261 (2021).
- ¹⁷ Qian, R. *et al.* Video-rate high-precision time-frequency multiplexed 3D coherent ranging. *Nature Communications* **13**, 1476 (2022).
- ¹⁸ Wang, S. *et al.* High-performance integrated laser based on thin-film lithium niobate photonics for coherent ranging. *Laser & Photonics Reviews* 2400224 (2024).
- ¹⁹ Behroozpour, B. *et al.* Electronic-photonic integrated circuit for 3D microimaging. *IEEE Journal of Solid-State Circuits* **52**, 161–172 (2016).
- ²⁰ Coddington, I., Giorgetta, F. R., Baumann, E., Swann, W. C. & Newbury, N. R. Characterizing fast arbitrary CW waveforms with 1500 THz/s instantaneous chirps. *IEEE Journal of Selected Topics in Quantum Electronics* **18**, 228–238 (2011).
- ²¹ Del’Haye, P., Arcizet, O., Gorodetsky, M. L., Holzwarth, R. & Kippenberg, T. J. Frequency comb assisted diode laser spectroscopy for measurement of microcavity dispersion. *Nature Photonics* **3**, 529–533 (2009).
- ²² Giorgetta, F., Coddington, I., Baumann, E., Swann, W. & Newbury, N. Fast high-resolution spectroscopy of dynamic continuous-wave laser sources. *Nature Photonics* **4**, 853–857 (2010).
- ²³ Baumann, E. *et al.* Comb-calibrated frequency-modulated continuous-wave lidar for absolute distance measurements. *Opt. Lett.* **38**, 2026–2028 (2013).
- ²⁴ Twayana, K. *et al.* Frequency-comb-calibrated swept-wavelength interferometry. *Opt. Express* **29**, 24363–24372 (2021).
- ²⁵ Shi, B. *et al.* Frequency-comb-linearized, widely tunable lasers for coherent ranging. *Photonics Research* **12**, 663–681 (2024).
- ²⁶ Yang, Q.-F. *et al.* Vernier spectrometer using counterpropagating soliton microcombs. *Science* **363**, 965–968 (2019).
- ²⁷ Jia, L. *et al.* Nonlinear calibration of frequency modulated continuous wave LIDAR based on a microresonator soliton comb. *Opt. Lett.* **46**, 1025–1028 (2021).
- ²⁸ Huber, R., Wojtkowski, M. & Fujimoto, J. Fourier domain mode locking (FDML): A new laser operating regime and applications for optical coherence tomography. *Opt. Express* **14**, 3225–3237 (2006).
- ²⁹ Grill, C. *et al.* Towards phase-stabilized fourier domain mode-locked frequency combs. *Communications Physics* **5**, 212 (2022).
- ³⁰ Jiang, Y., Karpf, S. & Jalali, B. Time-stretch LiDAR as a spectrally scanned time-of-flight ranging camera. *Nature Photonics* **14**, 14–18 (2020).
- ³¹ John, D. D. *et al.* Wideband electrically pumped 1050-nm MEMS-tunable VCSEL for ophthalmic imaging. *J. Lightw. Technol.* **33**, 3461–3468 (2015).
- ³² Chen, S. *et al.* High speed, long range, deep penetration swept source OCT for structural and angiographic imaging of the anterior eye. *Sci. Rep.* **12**, 992 (2022).
- ³³ Jung, E. J. *et al.* Characterization of FBG sensor interrogation based on a FDML wavelength swept laser. *Opt. Express* **16**, 16552–16560 (2008).
- ³⁴ Kranendonk, L. A. *et al.* High speed engine gas thermometry by Fourier-domain mode-locked laser absorption spectroscopy. *Opt. Express* **15**, 15115–15128 (2007).
- ³⁵ Ye, Z. *et al.* Foundry manufacturing of tight-confinement, dispersion-engineered, ultralow-loss silicon nitride photonic integrated circuits. *Photonics Research* **11**, 558–568 (2023).
- ³⁶ Zhang, X., Pouls, J. & Wu, M. C. Laser frequency

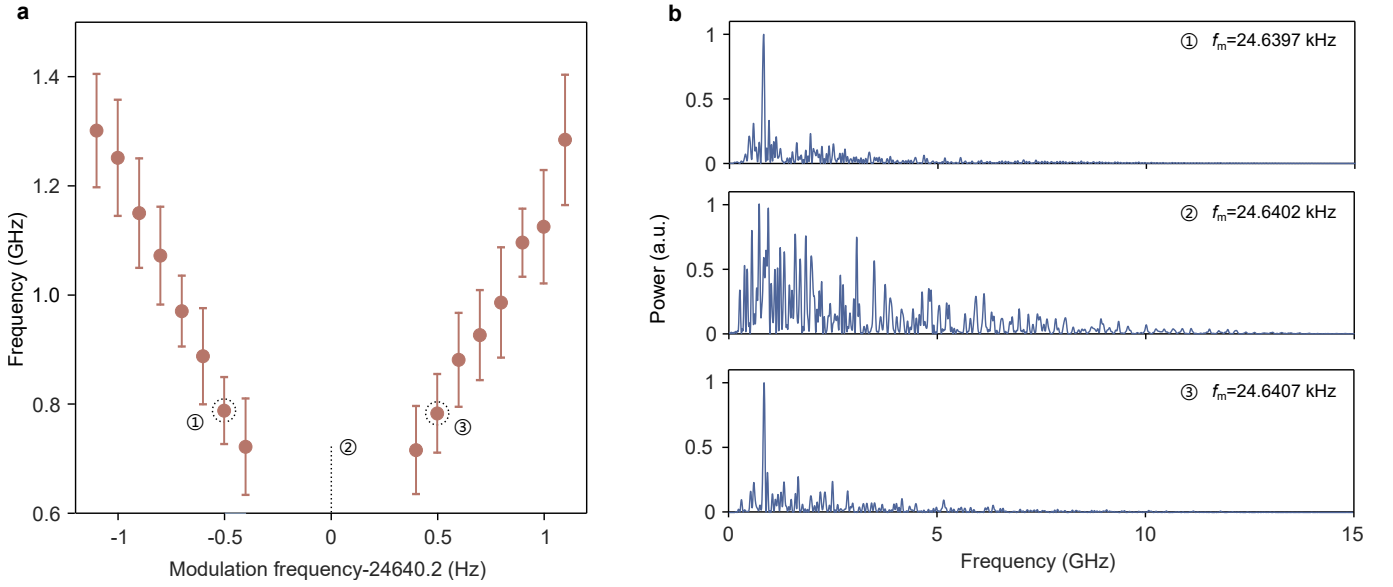
- sweep linearization by iterative learning pre-distortion for FMCW LiDAR. *Opt. Express* **27**, 9965–9974 (2019).
- ³⁷ Jeon, M. Y., Zhang, J. & Chen, Z. Characterization of Fourier domain mode-locked wavelength swept laser for optical coherence tomography imaging. *Opt. Express* **16**, 3727–3737 (2008).
- ³⁸ Caldwell, E. D., Sinclair, L. C., Newbury, N. R. & Deschenes, J.-D. The time-programmable frequency comb and its use in quantum-limited ranging. *Nature* **610**, 667–673 (2022).
- ³⁹ Kolb, J. P., Pfeiffer, T., Eibl, M., Hakert, H. & Huber, R. High-resolution retinal swept source optical coherence tomography with an ultra-wideband Fourier-domain mode-locked laser at MHz A-scan rates. *Biomedical Optics Express* **9**, 120–130 (2018).
- ⁴⁰ Pfeiffer, T. *et al.* Analysis of FDML lasers with meter range coherence. In *Optical Coherence Tomography and Coherence Domain Optical Methods in Biomedicine XXI*, vol. 10053, 125–130 (SPIE, 2017).
- ⁴¹ Stone, J. R. *et al.* Thermal and nonlinear dissipative-soliton dynamics in Kerr-microresonator frequency combs. *Phys. Rev. Lett.* **121**, 063902 (2018).
- ⁴² Liu, K. *et al.* Mitigating fast thermal instability by engineered laser sweep in AlN soliton microcomb generation. *Photonics Research* **11**, A10–A18 (2023).
- ⁴³ Huang, X. *et al.* Non-line-of-sight imaging and vibrometry using a comb-calibrated coherent sensor. *Phys. Rev. Lett.* **132**, 233802 (2024).
- ⁴⁴ Jia, L. *et al.* Nonlinear calibration of frequency modulated continuous wave LIDAR based on a microresonator soliton comb. *Opt. Lett.* **46**, 1025–1028 (2021).
- ⁴⁵ Zheng, J. *et al.* High-precision silicon-integrated frequency-modulated continuous wave LiDAR calibrated using a microresonator. *ACS Photonics* **9**, 2783–2791 (2022).
- ⁴⁶ Huang, X., Hong, Y., Li, Z.-P. & Xu, F. Frequency-modulated continuous-wave 3D imaging with high photon efficiency. *Opt. Lett.* **47**, 3568–3571 (2022).
- ⁴⁷ Liu, C. *et al.* Highly-linear and wavelength-tunable frequency-modulated continuous-wave hybrid-integrated laser. *Laser & Photonics Reviews* 2300882 (2024).
- ⁴⁸ Martin, A. *et al.* Photonic integrated circuit-based FMCW coherent LiDAR. *J. Lightw. Technol.* **36**, 4640–4645 (2018).
- ⁴⁹ DiLazaro, T. & Nehmetallah, G. Large-volume, low-cost, high-precision FMCW tomography using stitched DFBs. *Opt. Express* **26**, 2891–2904 (2018).
- ⁵⁰ Tang, L., Li, L., Li, J. & Chen, M. Hybrid integrated ultralow-linewidth and fast-chirped laser for FMCW LiDAR. *Opt. Express* **30**, 30420–30429 (2022).
- ⁵¹ Wang, Y. *et al.* Laser feedback frequency-modulated continuous-wave LiDAR and 3-D imaging. *IEEE Trans. Instrum. Meas.* **72**, 7002309 (2023).
- ⁵² He, B. *et al.* Massively parallel FMCW lidar with cm range resolution using an electro-optic frequency comb. *Opt. Lett.* **48**, 3621–3624 (2023).
- ⁵³ Mrokon, A., Oehler, J. & Breunig, I. Continuous adiabatic frequency conversion for FMCW-LiDAR. *Sci. Rep.* **14**, 4990 (2024).
- ⁵⁴ Lukashchuk, A., Riemensberger, J., Karpov, M., Liu, J. & Kippenberg, T. J. Dual chirped microcomb based parallel ranging at megapixel-line rates. *Nature Communications* **13**, 3280 (2022).
- ⁵⁵ Dong, Y., Zhu, Z., Tian, X., Qiu, L. & Ba, D. Frequency-modulated continuous-wave LIDAR and 3D imaging by using linear frequency modulation based on injection locking. *J. Lightw. Technol.* **39**, 2275–2280 (2021).
- ⁵⁶ Okano, M. & Chong, C. Swept Source Lidar: simultaneous FMCW ranging and nonmechanical beam steering with a wideband swept source. *Opt. Express* **28**, 23898–23915 (2020).
- ⁵⁷ Hariyama, T., Sandborn, P. A., Watanabe, M. & Wu, M. C. High-accuracy range-sensing system based on FMCW using low-cost VCSEL. *Opt. Express* **26**, 9285–9297 (2018).
- ⁵⁸ Han, Y. *et al.* High-speed two-dimensional spectral-scanning coherent LiDAR system based on tunable VCSEL. *J. Lightw. Technol.* **41**, 412–419 (2022).
- ⁵⁹ Zhang, X., Pouls, J. & Wu, M. C. Laser frequency sweep linearization by iterative learning pre-distortion for FMCW LiDAR. *Opt. Express* **27**, 9965–9974 (2019).
- ⁶⁰ Ula, R. K., Noguchi, Y. & Iiyama, K. Three-dimensional object profiling using highly accurate FMCW optical ranging system. *J. Lightw. Technol.* **37**, 3826–3833 (2019).



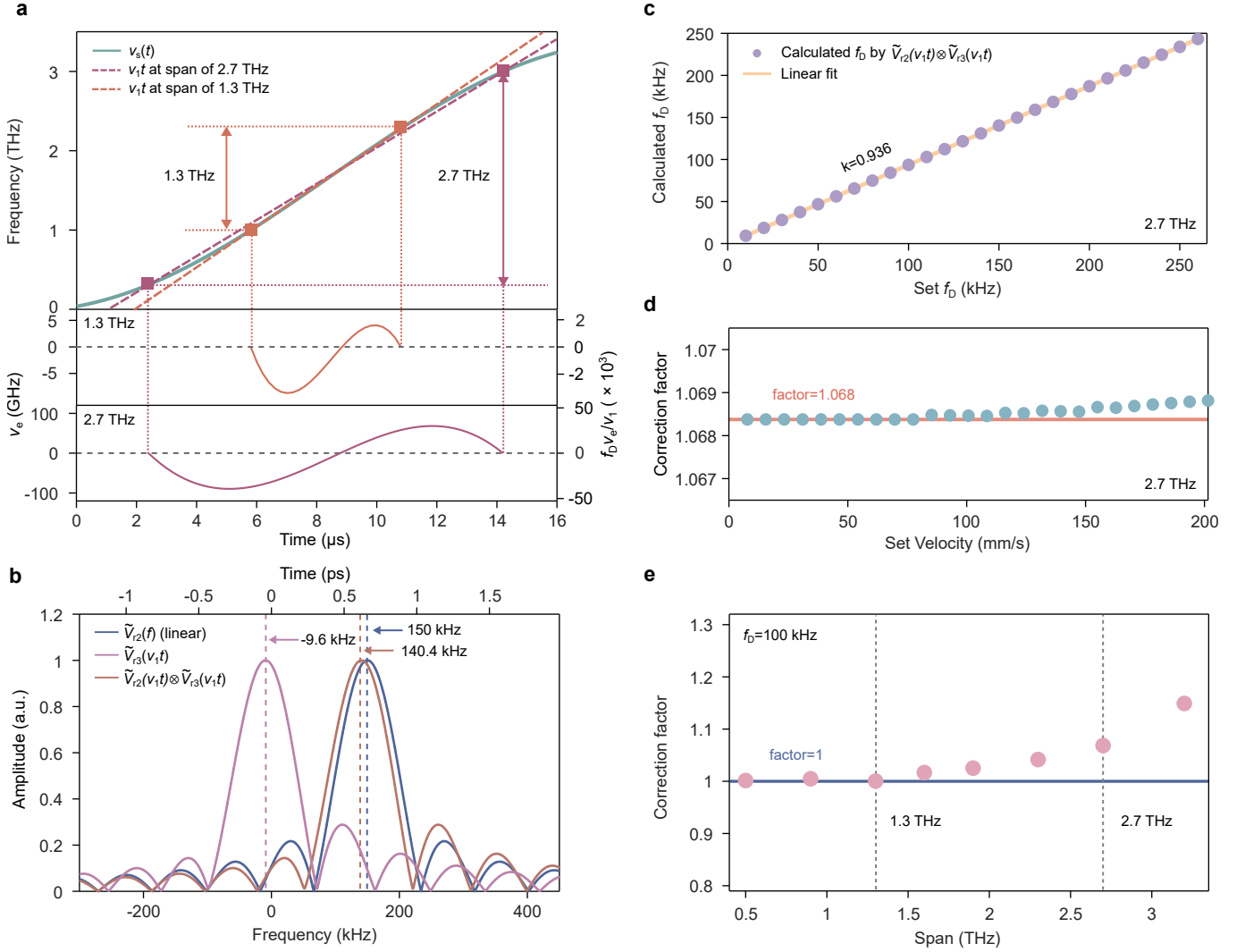
Extended Data Fig. 1: Linearity measurement for the FDML LiDAR. **a**, Experimental setup for the ranging linearity measurement. By mounting the mirrors on a linear translation stage, we characterized the linearity measurement accuracy of the FDML LiDAR. The movement of the target was calibrated by a laser interferometer. To cancel the fibre length fluctuations, we added a reference mirror in this setup too. Circ.: circulator, Col.: collimator, BS: beam filter, RM: reference mirror, MMs: measurement mirrors, BPD: balanced photodetector. **b**, Top: FDML LiDAR measured distance change versus the laser interferometer calibrated distance change. The measurement data were recorded by the 33 GHz Tektronix oscilloscope (bandwidth set at 24 GHz). Bottom: The residual error between the FDML LiDAR and the interferometer measured results. The standard deviation is 0.2 μm. **c**, The ranging linearity measurements recorded by the 8 GHz Keysight oscilloscope. The standard deviation of the residual error is 1.0 μm.



Extended Data Fig. 2: Frequency calibration process. **a**, We first selected a segment of the recorded calibration signal by a $4.6 \mu\text{s}$ window. **b**, The segmented data was Fourier transformed and bandpass filtered (shaded boxes represent the passband). **c**, The bandpass filtered spectrum was inverse Fourier transformed back to the domain. The phase of the signal was retrieved by the Hilbert transform (blue curve). The retrieved phase was further smoothed in a 2 ns window (red curve). **d**, The instantaneous frequency was derived as the derivative of the phase versus time. The blue and red curves show the frequency without and with phase smoothing, respectively. The inset is a zoom in of the dashed box region. **e**, Retrieved frequency in the full sweep span. The frequencies were calibrated by 74 microcomb lines and were wrapped by f_r . The shaded box corresponds to the filtered pump and adjacent lines. **f**, The retrieved frequencies were further unwrapped by the 50.08 GHz comb line spacing (dots). The unwrapped frequencies were fitted by a 9th-order polyfit. This fit was used to resample the time domain signal for ranging.



Extended Data Fig. 3: Occurring frequency of the frequency spurs in the FDML laser. **a**, Measured occurring frequency of the frequency spurs (abrupt frequency changes shown in Fig. 2b) under different modulation frequencies. The frequency is about 1 GHz and is quite sensitive to the modulation frequency. The middle of the figure corresponds to a regime where there is no obvious occurring frequency. The error bar corresponds to the standard deviation of the occurring frequency in multiple measurements. **b**, Examples of the power spectra of the measured instantaneous frequency after removing the smoothed frequency change (e.g., frequency in the light curve minus the dark curve in Fig. 2b). At a modulation frequency marked by 1 or 3 in panel **a**, the frequency spurs occur at a well-defined frequency. At a modulation frequency marked by 2, the power spectrum is broad, and there is no well-defined frequency.



Extended Data Fig. 4: Correction factor for velocity measurement with nonlinear frequency sweep. **a**, The green curve is the 9th-order polyfit of the calibrated frequency sweep $\nu_s(t)$. We used linear fits $\nu_1 t$ to approximate the nonlinear frequency sweep, where ν_1 is the overall chirp rate and was calculated as the frequency difference between the ending moment ($t=T$) and the starting moment ($t=0$) divided by the sweep time T (see Methods). Since the frequency sweeps in a nonlinear way, there is an error frequency ν_e between ν_s and the linear fits $\nu_1 t$, which is plotted in the bottom panels. The error frequency ν_e becomes much larger when the 2.7 THz bandwidth was used. **b**, In a linear sweep case, the ranging spectrum has a peak centered at the set $f_D=150$ kHz by Fourier transform the time domain data directly ($\tilde{V}_{r2}(f)$ and dark blue curve). In a nonlinear sweep case, data resampling is needed, and $\tilde{V}_{r3}(t)$ in Eq. 10 should be corrected to locate f_D . By using the calibrated $\nu_e(t)$ for the 2.7 THz bandwidth shown in panel **a**, we can calculate $\tilde{V}_{r3}(t)$ (thus, $\tilde{V}_{r3}(\nu_1 t)$). The calculated $\tilde{V}_{r3}(\nu_1 t)$ corresponds to a peak at -9.6 kHz (light pink curve). Due to this shift, the center of ranging spectrum calculated by $\tilde{V}_{r2}(\nu_1 t) \otimes \tilde{V}_{r3}(\nu_1 t)$ is located at 140.4 kHz (brick red curve), as opposed to the set 150 kHz. Thus, a correction factor $\alpha=1.068$ should be multiplied to the measured frequency shift to locate f_D . **c**, Calculated f_D under different set velocity and f_D when using the $\nu_e(t)$ with 2.7 THz bandwidth in panel **a**. **d**, Correction factor α between the calculated and set f_D shown in panel **c**. **e**, Correction factor when selecting different optical bandwidths in $\nu_s(t)$ in panel **a** for FMCW measurements, assuming a prior knowledge of $f_D=100$ kHz.

Extended Data Table 1: Detailed comparison with other FMCW LiDARs

No.	Type	Resolution	Normalized precision	Chirp rate	Update rate	Velocity uncertainty	Vel. uncert./ Chirp rate ^a	Ref.
1	ECDL	75 μm	2.5 $\mu\text{m} \cdot \sqrt{\text{s}}$	1.0×10^{14} Hz/s	100 Hz	N/A	N/A	43
2	ECDL	60 μm	4.9 $\mu\text{m} \cdot \sqrt{\text{s}}$	1.25×10^{13} Hz/s	5 Hz	N/A	N/A	44
3	ECDL	60 μm	0.21 $\mu\text{m} \cdot \sqrt{\text{s}}$	1.0×10^{13} Hz/s	200 Hz	N/A	N/A	45
4	ECDL	12 mm	N/A	6.25×10^{12} Hz/s	500 Hz	N/A	N/A	46
5	ECDL	214 mm	1.3 mm $\cdot \sqrt{\text{s}}$	1.4×10^{12} Hz/s	1 kHz	N/A	N/A	47
6	DFB	280 mm	N/A	1.6×10^{13} Hz/s	1.9 kHz	N/A	N/A	48
7	DFB	17 mm	N/A	1.1×10^{14} Hz/s	6.25 kHz	N/A	N/A	4
8	DFB array	27 μm^b	0.25 $\mu\text{m} \cdot \sqrt{\text{s}}$	1.8×10^{15} Hz/s	333 Hz	N/A	N/A	49
9	DBR	1.2 mm	17.9 nm $\cdot \sqrt{\text{s}}$	2.2×10^{16} Hz/s	180 kHz	N/A	N/A	19
10	DBR	2.8 mm	0.3 $\mu\text{m} \cdot \sqrt{\text{s}}$	7.5×10^{14} Hz/s	16 kHz	N/A	N/A	17
11	PZT mod.	125 mm	N/A	1.7×10^{15} Hz/s	800 kHz	N/A	N/A	14
12	PZT mod.	35 mm	0.27 mm $\cdot \sqrt{\text{s}}$	8.4×10^{14} Hz/s	10 kHz	N/A	N/A	50
13	PZT mod.	5.2 mm	1.1 $\mu\text{m} \cdot \sqrt{\text{s}}$	1.1×10^{13} Hz/s	80 Hz	60 $\mu\text{m}/\text{s}$^c	5.4 $\mu\text{m}/\text{THz}$	51
14	EO mod.	59 mm	31.6 $\mu\text{m} \cdot \sqrt{\text{s}}$	4.4×10^{16} Hz/s	10 MHz	N/A	N/A	12
15	EO mod.	87 mm	4.9 $\mu\text{m} \cdot \sqrt{\text{s}}$	3.44×10^{16} Hz/s	5 MHz	54 mm/s	1.6 $\mu\text{m}/\text{THz}$	18
16	EO mod.	125 mm	N/A	1.2×10^{16} Hz/s	10 MHz	N/A	N/A	15
17	EO mod.	15.4 mm	5.6 $\mu\text{m} \cdot \sqrt{\text{s}}$	1.17×10^{16} Hz/s	390 kHz	N/A	N/A	52
18	EO mod.	220 mm	N/A	1.0×10^{16} Hz/s	20 MHz^d	N/A	N/A	53
19	EO mod.	80 mm	N/A	3.6×10^{14} Hz/s	100 kHz	0.1 m/s	277 $\mu\text{m}/\text{THz}$	54
20	EO mod.	25 mm	N/A	6.0×10^{13} Hz/s	5 kHz	7.8 mm/s	130 $\mu\text{m}/\text{THz}$	55
21	EO mod.	37.5 mm	74 $\mu\text{m} \cdot \sqrt{\text{s}}$	4.7×10^{12} Hz/s	588 Hz	1 mm/s	213 $\mu\text{m}/\text{THz}$	16
22	MEMS	420 μm	N/A	1.1×10^{17} Hz/s	10 kHz	N/A	N/A	56
23	MEMS	330 μm	61 nm $\cdot \sqrt{\text{s}}$	1.7×10^{16} Hz/s	10 kHz	N/A	N/A	57
24	MEMS	3.5 mm	22.4 $\mu\text{m} \cdot \sqrt{\text{s}}$	8.1×10^{15} Hz/s	8 kHz	N/A	N/A	58
25	MEMS	130 μm	2.5 nm $\cdot \sqrt{\text{s}}$	3.15×10^{15} Hz/s	1 kHz	N/A	N/A	23
26	MEMS	970 μm	N/A	1.55×10^{15} Hz/s	5 kHz	4 mm/s	2.6 $\mu\text{m}/\text{THz}$	59
27	MEMS	460 μm	85.5 nm $\cdot \sqrt{\text{s}}$	1.4×10^{15} Hz/s	1 kHz	N/A	N/A	60
28	FDML	55 μm	0.27 nm $\cdot \sqrt{\text{s}}$	3.2×10^{17} Hz/s	24.6 kHz	0.4 mm/s	1.8 nm/THz	This work

ECDL, external cavity diode laser; DFB, distributed feedback laser; DBR, distributed Bragg reflector laser; PZT mod., frequency tuning achieved via piezoelectric tuning; EO mod., frequency tuning achieved via electro-optic modulation; MEMS, the laser is micro-electro-mechanically tuned.

^aSince velocity uncertainty is impacted by the overall chirp rate ν_1 (Methods), this metric is also evaluated.

^bFine resolution achieved by stitching an array of 12 DFB lasers; a single DFB laser achieves a resolution of 333 μm .

^cLow velocity measurement uncertainty achieved with low chirp rate.

^dFrequency sweep range is 0.5 GHz.